

## **Supplementary Materials:**

# **The slow slip event cycle along the Izmit segment of the North Anatolian Fault**

Estelle Neyrinck<sup>a</sup>, Baptiste Rousset<sup>a</sup>, Cécile Doubre<sup>a</sup>, Luis Rivera<sup>a</sup>, Cécile Lasserre<sup>b</sup>,  
Marie-Pierre Doin<sup>c</sup>, Philippe Durand<sup>d</sup>, Roger Bilham<sup>e</sup>, Ziyadin Çakir<sup>f</sup>, FLATSIM Working  
Group<sup>g</sup>

<sup>a</sup> Institut Terre et Environnement de Strasbourg, Université de Strasbourg (UMR 7063), Strasbourg, 67000, France

<sup>b</sup> LGL-TPE, CNRS, Univ Lyon, ENSL, Lyon, France

<sup>c</sup> ISTerre, CNRS, Université Grenoble Alpes, Grenoble, France

<sup>d</sup> CNES, Toulouse, France

<sup>e</sup> CIRES and Geological Sciences, University of Colorado Boulder, Boulder, CO, USA

<sup>f</sup> Department of Geology, Istanbul Technical University, Istanbul, Türkiye

<sup>g</sup> doi:10.24400/253171/FLATSIM2020

## **Contents**

<b>1 InSAR analysis</b>	<b>1</b>
1.1 InSAR data presentation . . . . .	1
1.2 Extraction of the tectonic signal by Independent Component Analysis (ICA) . . . . .	3
1.3 Mean velocities and seasonal signals analysis . . . . .	6
1.4 Fault relative displacement . . . . .	11
1.5 Slip inference at depth . . . . .	13
<b>2 Discussion materials</b>	<b>24</b>

# 1 InSAR analysis

## 1.1 InSAR data presentation

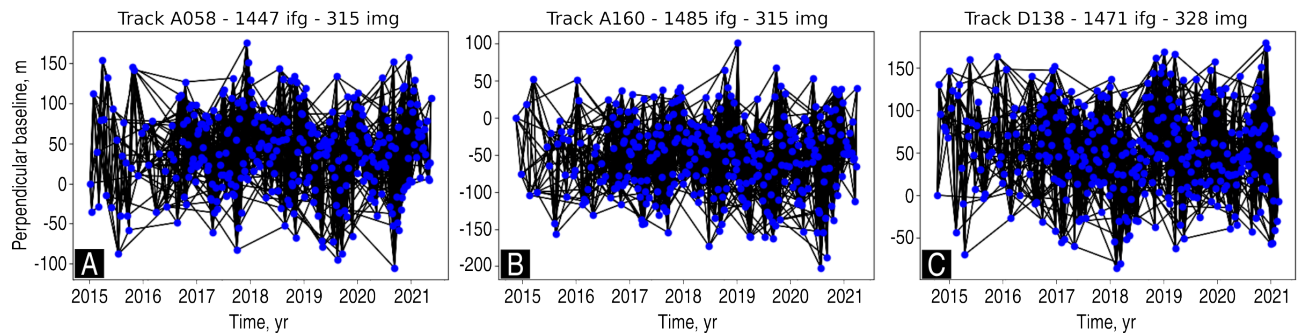


Figure S1: Interferogram networks for the tracks A058 (A), A160 (B) and D138 (C). *ifg* and *img* stand for interferograms and images, respectively.

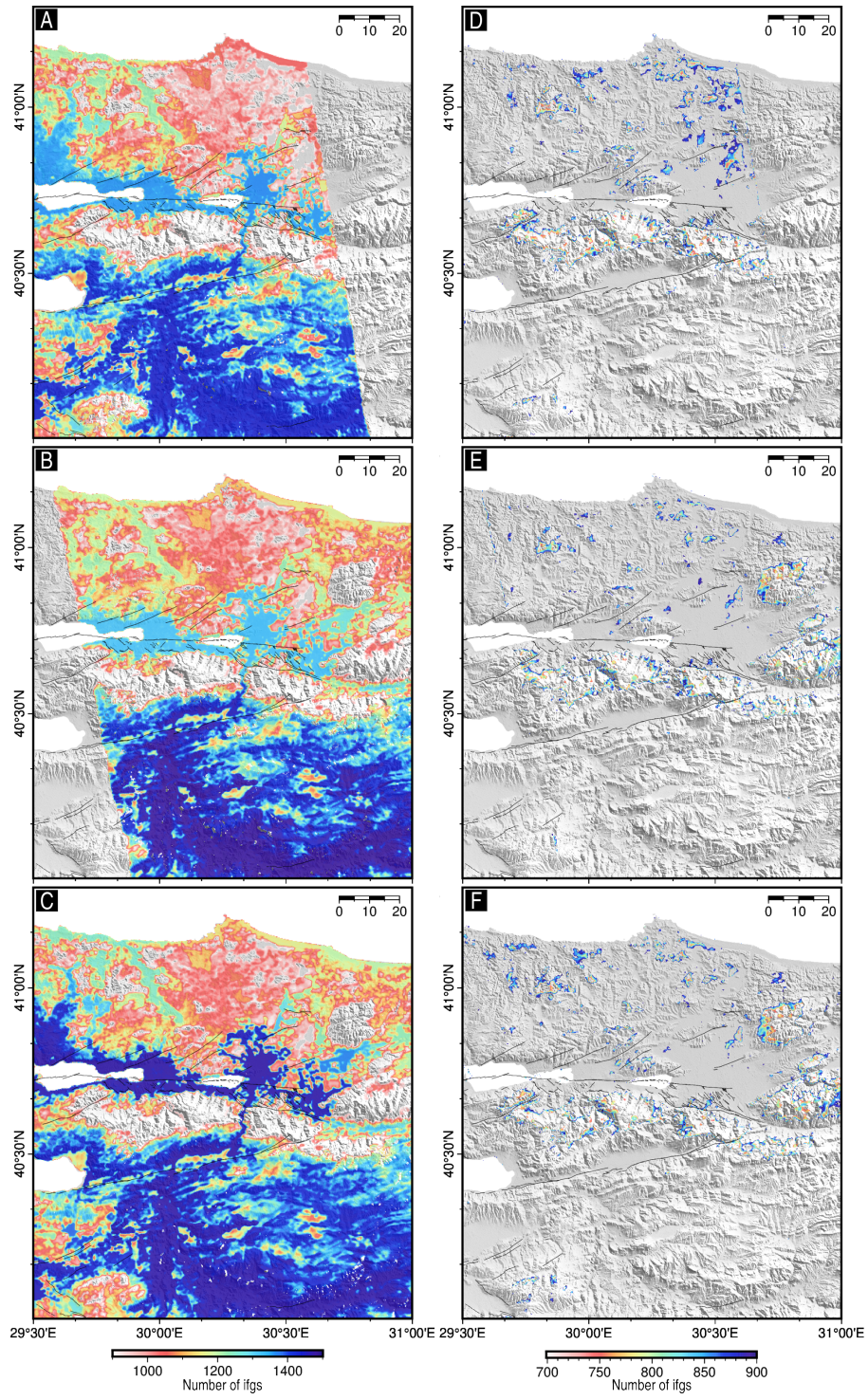


Figure S2: Number of interferograms (*ifgs*) per pixel for each track above the threshold of 900 interferograms (A-C) and below (D-F). Number of interferograms for the tracks A058, A160 and D138 correspond to the maps (A,D), (B,E) and (C,F), respectively.

## 1.2 Extraction of the tectonic signal by Independent Component Analysis (ICA)

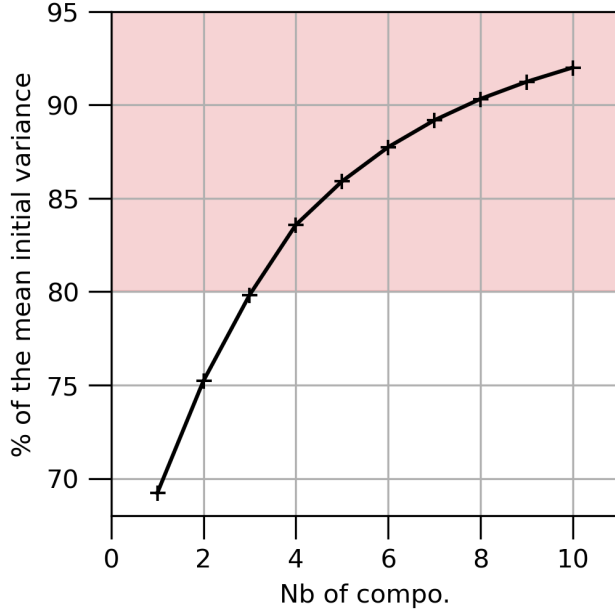


Figure S3: Comparison of the variance of the reconstructed data based on the ICA sources with the variance of the InSAR time series, as a function of the number of components used for the ICA. The results are given as a percentage of the InSAR variance explained by the ICA sources. The red area corresponds to the area within at least 80% of the InSAR data is explained by the components. In order to get a compromise between the reconstructed variance and the number of IC components, we chose to use three components.

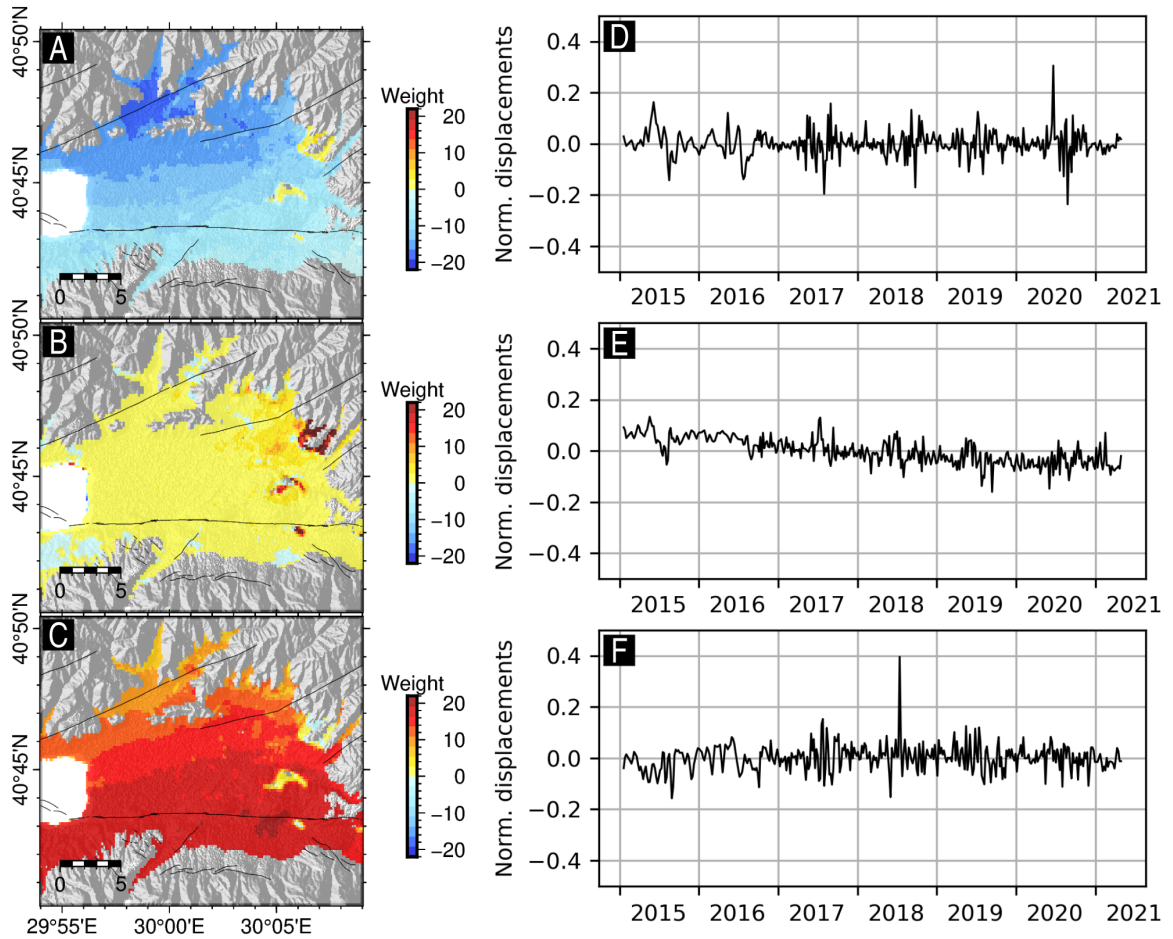


Figure S4: Three sources extracted by the FastICA algorithm. (A,B,C) Weight per pixels for each sources, corresponding to the mixing matrix. (D,E,F) Temporal sources extracted corresponding to each map. The A and C maps show patterns with high amplitudes associated with high standard deviation on summer (D and F). The maps of these components do not have patterns related to the fault location.

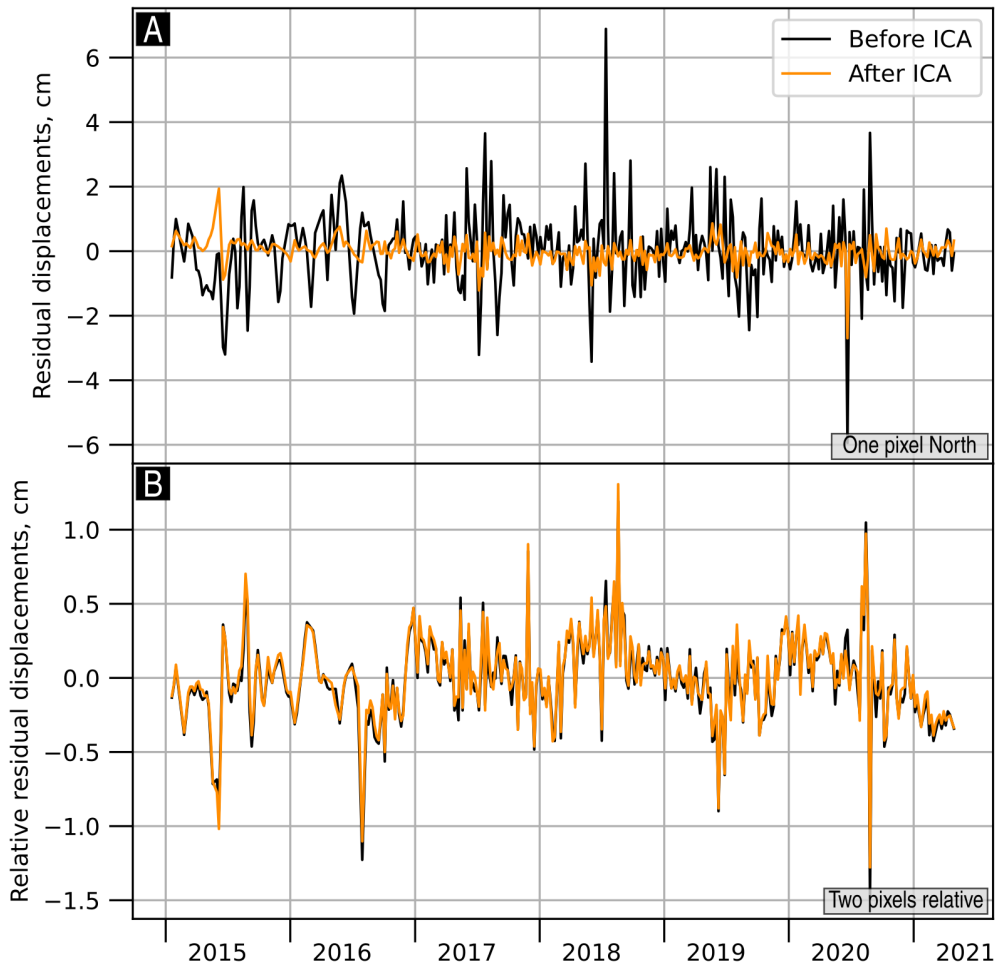


Figure S5: Examples of residual time series before (in black) and after (in orange) subtraction of the IC components. (A) Residual time series of one pixel located North of the fault ( $40.73^{\circ}N 29.99^{\circ}E$ ). (B) Relative residual time series computed using the previous pixel and a pixel located South of the fault ( $40.73^{\circ}N 29.99^{\circ}E$ ). Note that the ICA enables to reduce the variance of the time series by about 89.6% (A), without decreasing the tectonic signal as shown by the relative analysis close to the fault (B).

### 1.3 Mean velocities and seasonal signals analysis

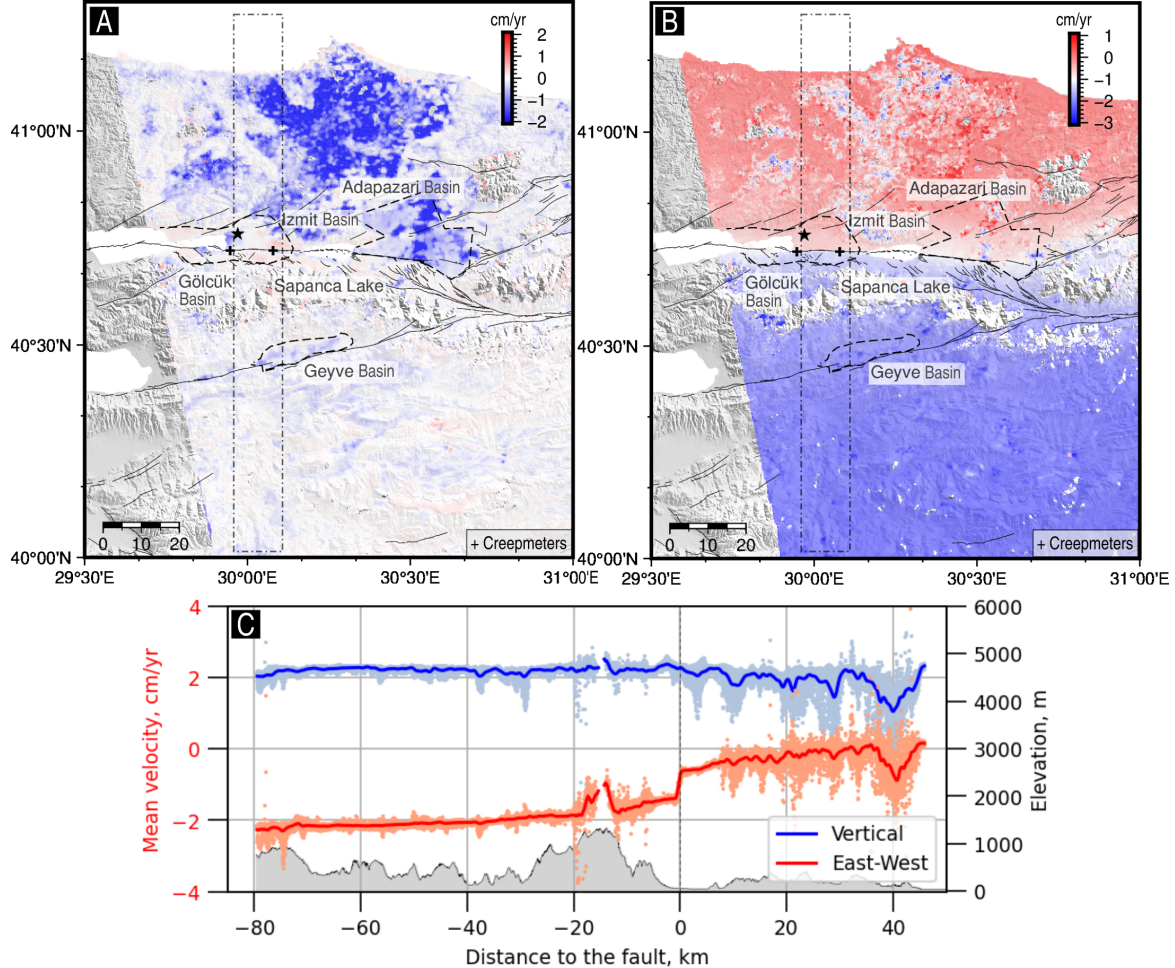


Figure S6: Mean horizontal and vertical velocities of the cropped zone computed after HV decomposition of the tracks A160 and D138, and after GNSS referencing. (A) Mean vertical velocity with in red and blue up and down displacements, respectively. The dotted lines highlight the major Quaternary basins named by the main city within them, Gölcük, Izmit, Adapazarı and Geyve. The fault network is shown by the black lines. The black star is the 1999 Izmit earthquake epicenter and the two black crosses correspond to the Izmit (West) and Tepetarla (East) creepmeters. (B) Mean East-West velocity with in red and blue eastward and westward displacements, respectively. (C) Fault-perpendicular velocity profiles (dot-dashed rectangle in the upper maps) are plotted relatively to the mean elevation of the zone. The lines correspond to the mean average of the data, red and blue corresponding to the East-West and vertical velocities respectively.

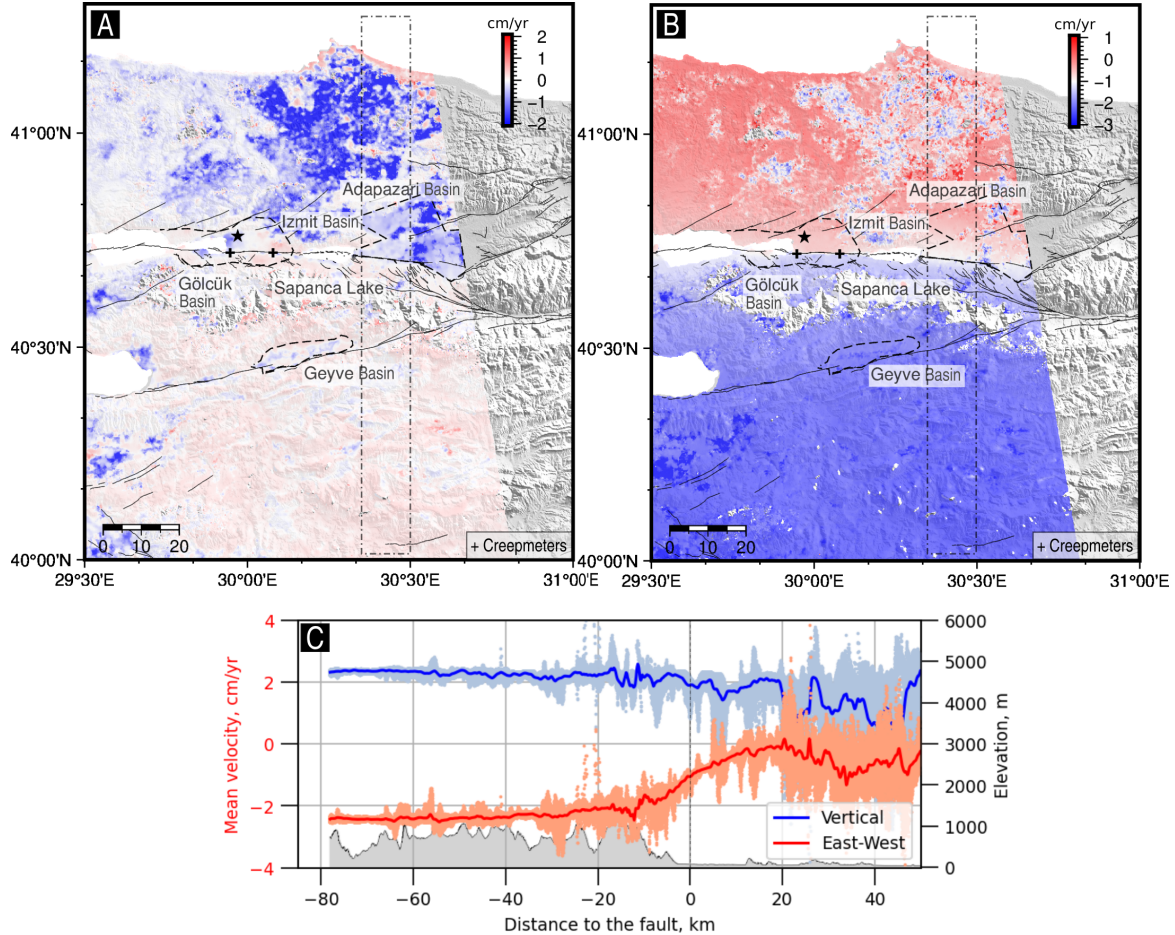


Figure S7: Mean horizontal and vertical velocities of the cropped zone computed after HV decomposition of the tracks A058 and D138, and after GNSS referencing. (A) Mean vertical velocity with red and blue up and down displacements, respectively. The dotted lines highlight the major Quaternary basins named by the main city within them, Gölçük, Izmit, Adapazari and Geyve. The fault network is shown by the black lines. The black star is the 1999 Izmit earthquake epicenter and the two black crosses correspond to the Izmit (West) and Tepetarla (East) creepmeters. (B) Mean East-West velocity with red and blue eastward and westward displacements, respectively. (C) Fault-perpendicular velocity profiles (dot-dashed rectangle in the upper maps) are plotted relatively to the mean elevation of the zone. The lines correspond to the mean average of the data, red and blue corresponding to the East-West and vertical velocities respectively.

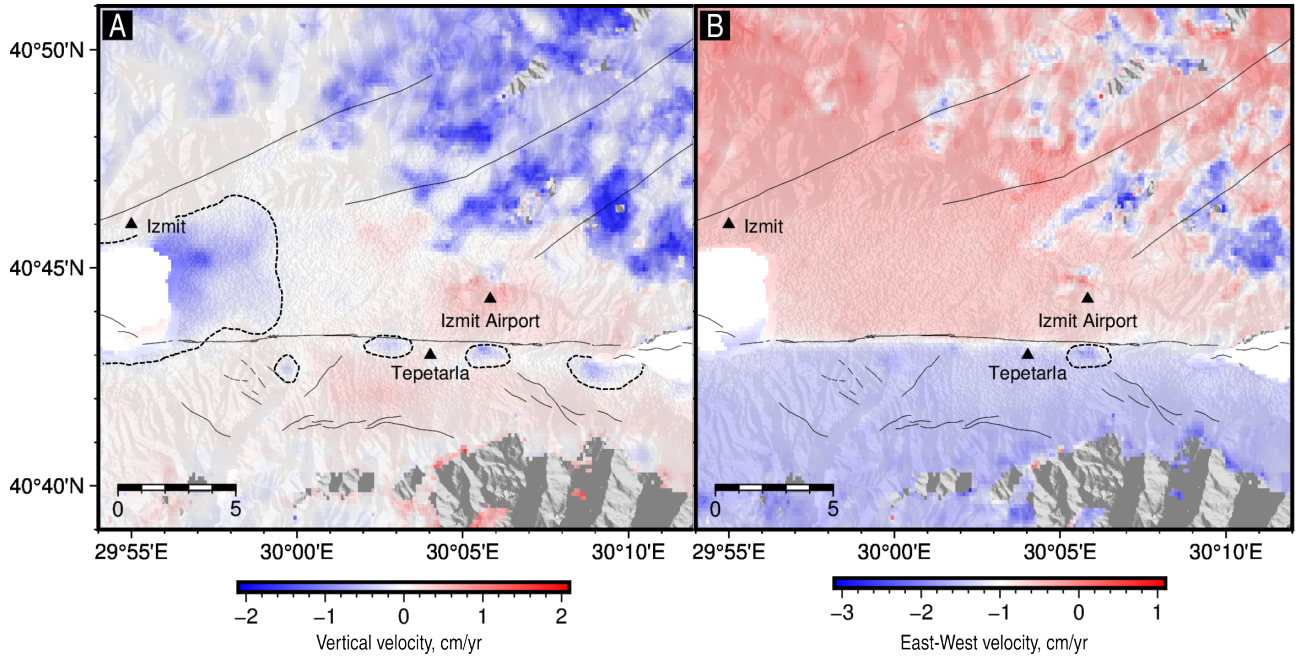


Figure S8: Mean East-West horizontal and vertical surface velocities on the Izmit basin computed after the HV decomposition of the tracks A058 and D138, and after GNSS referencing. (A) Mean vertical velocity in  $cm/yr$  with in red and blue up and down displacements, respectively. The dotted lines highlight areas affected by a strong downward motion. The three eastern areas are correlated with swamps, mapped by [Barka \(2002\)](#). (B) Mean East-West velocity in  $cm/yr$  with in red and blue eastward and westward displacements, respectively. The dotted ellipse highlights an area located South of the surface fault trace and affected by a stronger westward motion, corresponding to one of the swamps. The fault network is shown by the black lines.

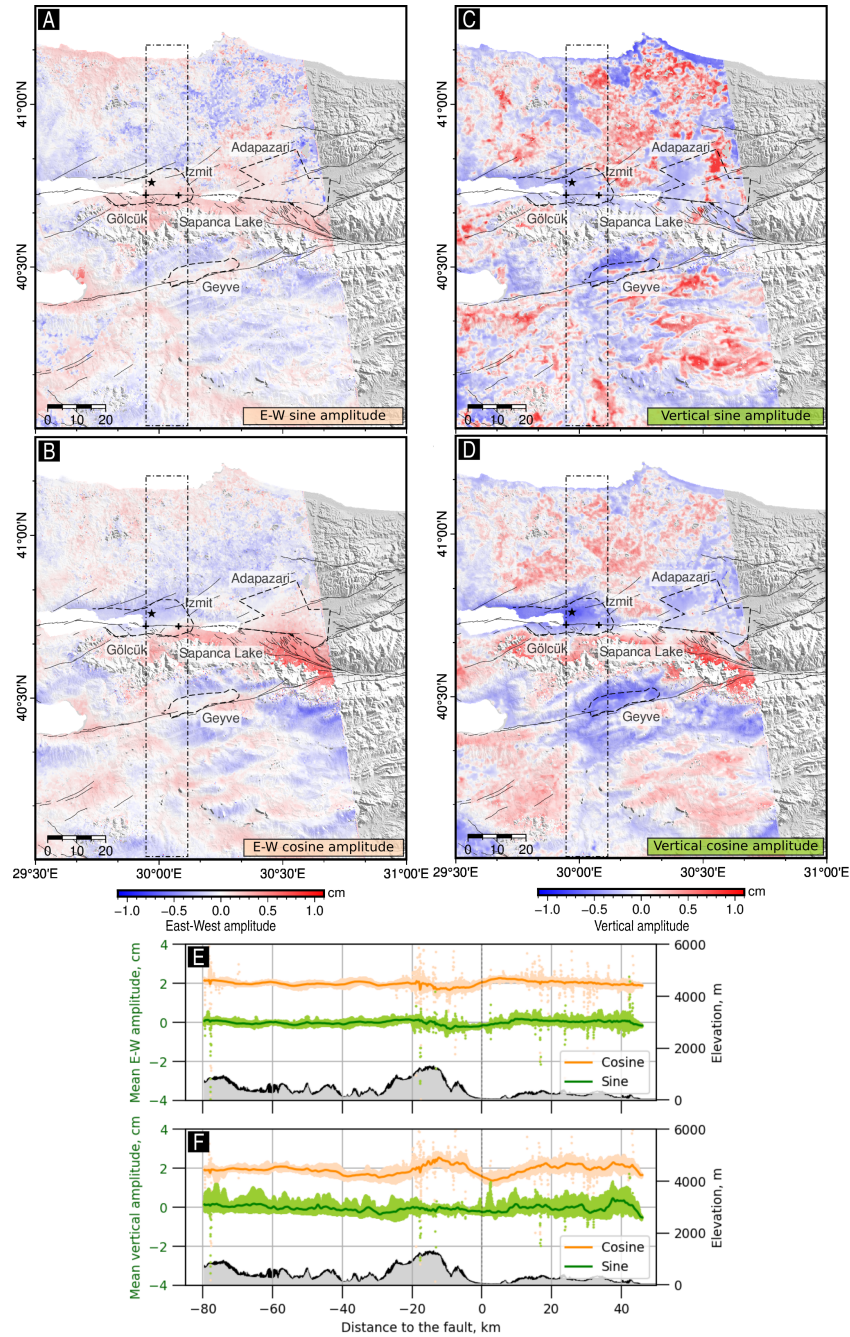


Figure S9: East-West (A,B) and vertical (C,D) seasonal amplitudes obtained from the *TA058-D138* decomposition. The positive and negative values (red and blue) of the East-West amplitudes correspond to eastward and westward deformation amplitude, respectively, and the positive and negative values of the vertical amplitudes correspond to upward and downward deformation amplitude, respectively. (E,F) Perpendicular to the fault profiles corresponding to the pixels within the dashed rectangle on the above maps.

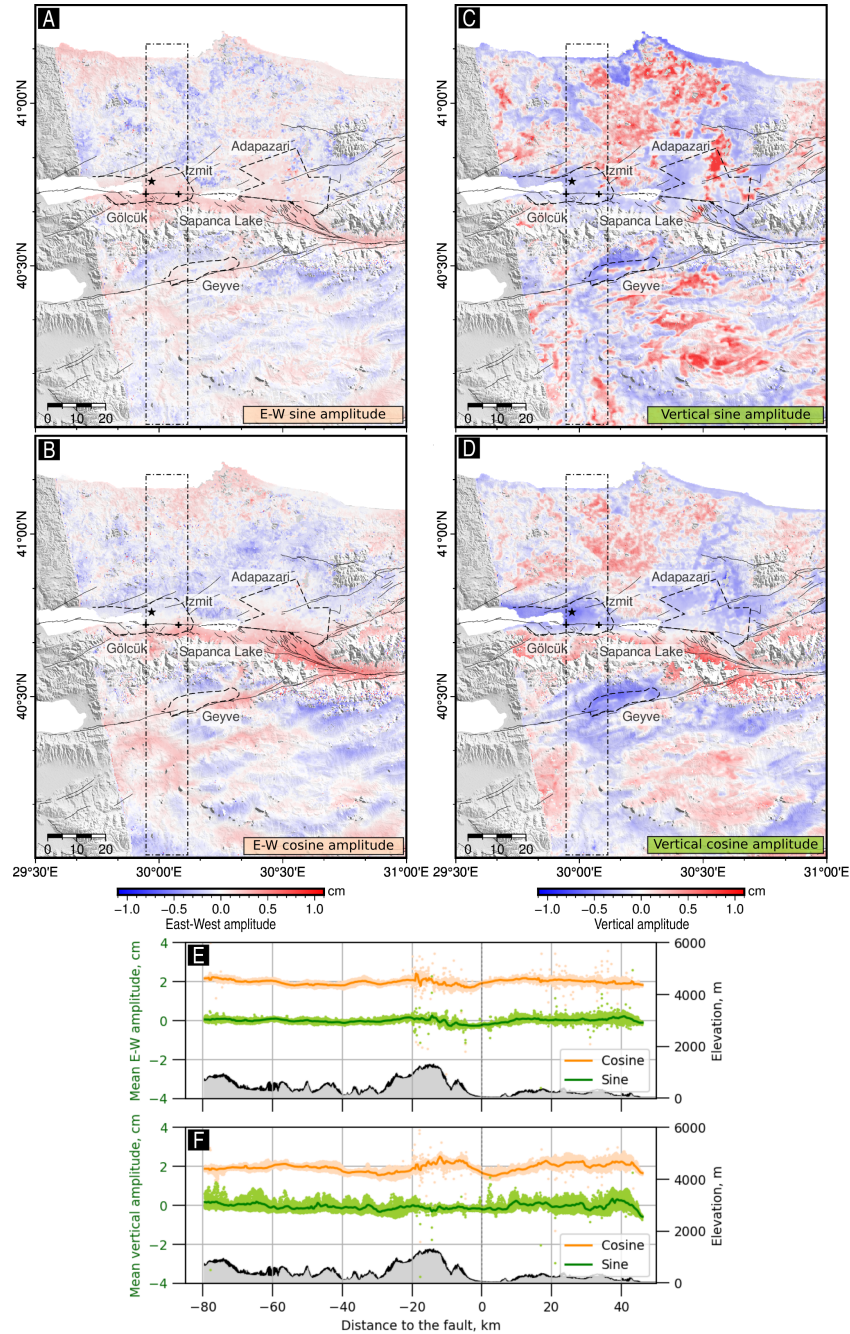


Figure S10: East-West (A,B) and vertical (C,D) seasonal amplitudes obtained from the *TA160-D138* decomposition. The legend is the same as for figure [Figure S8](#).

The amplitudes of the seasonal amplitudes (figures S8 and S9) are two to three times larger on the vertical components than on the horizontal East-West ones. The spring/autumn cycles (term *C*) present higher frequency contents than the summer/winter cycles (term *D*), with high amplitudes north of the NAF in crop areas, likely related to surface moisture. The large-scale annual deformation cycles are more pronounced along the cosine components (summer/winter cycles) and are correlated with the topography, with larger amplitudes in the valleys. The three sedimentary basins of Izmit, Adapazari and Geyve have particularly large seasonal vertical deformation.

#### 1.4 Fault relative displacement

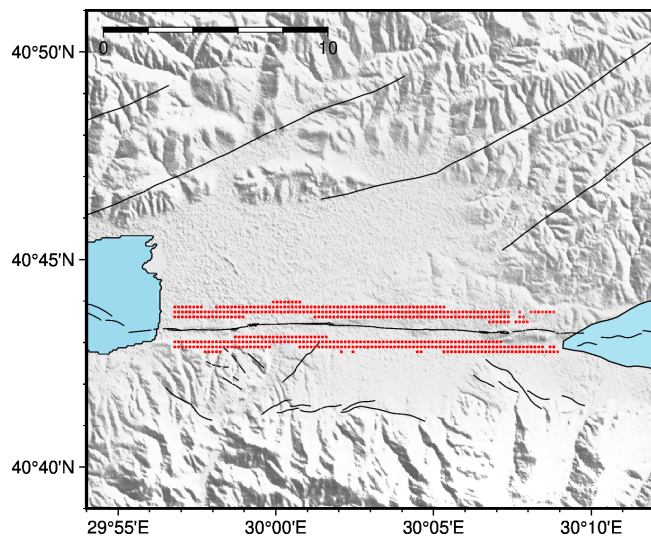


Figure S11: Map centered on the Izmit basin with the location of the pixels used for the calculation of the relative displacement rates. The pixels are pointed out with red dots, on both side of the Izmit segment.

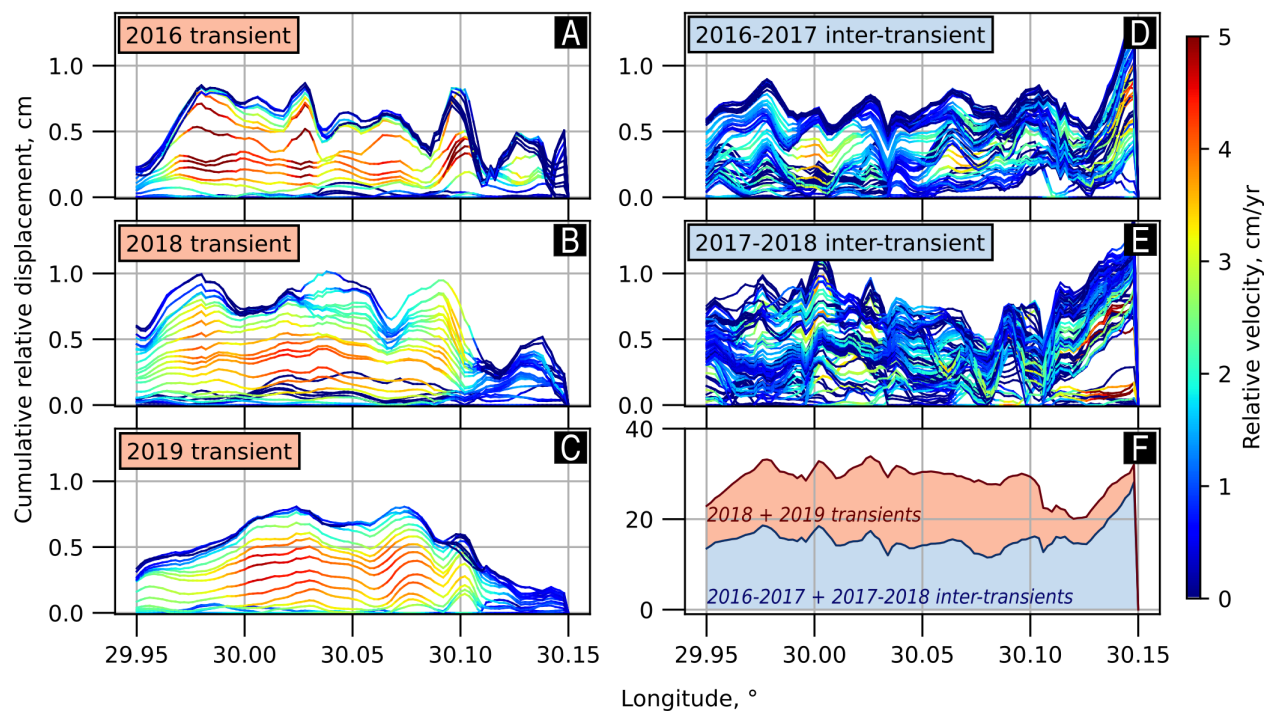


Figure S12: Cumulative relative displacement using the data from the *TA160-D138* HV decomposition recorded during (A,B,C) and in between (D,E) three transient events: in December 2016, in March 2018 and in November 2019. The two inter-transient periods are between the 2016 (from the October 10, 2016 to the January 20, 2017) and 2018 (from the January 1<sup>st</sup>, 2018 to the May 20, 2018) events and 2018 and 2019 (from the October 10, 2019 to the January 10, 2020) events. (F) Sum of the relative cumulative displacement during the transient (red) and inter-transient (blue) periods.

## 1.5 Slip inference at depth

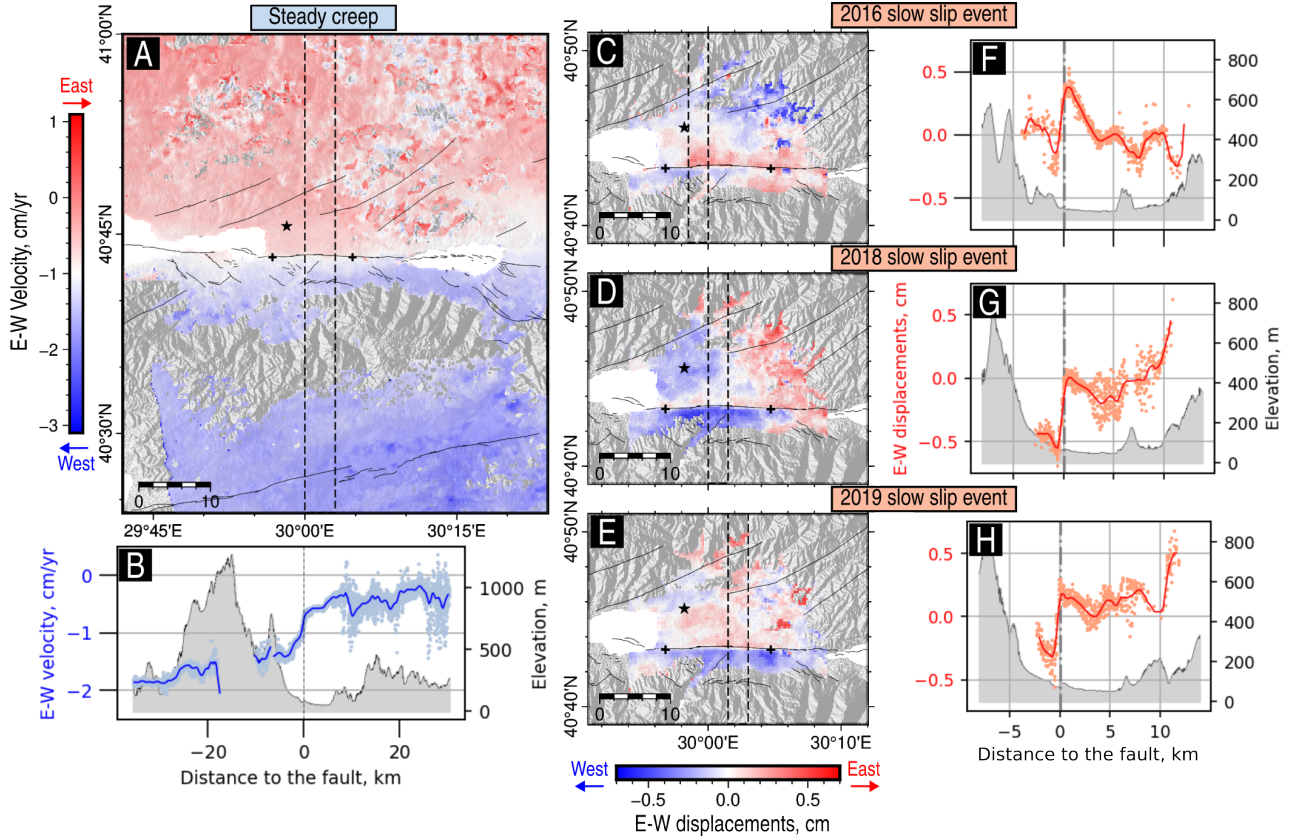


Figure S13: East-West velocity field during the steady creep periods and East-West static offsets during the transient slow slip events from the *TA160-D138* HV decomposition. (A) Surface velocity computed during the steady creep periods. (B) Fault-perpendicular profile (location on A with the dashed lines) of the East-West velocity and of the mean elevation. (C-E) Static displacements offsets estimated during the three transient slow slip events in 2016 (C), 2018 (D) and 2019 (E). (F-H) Associated fault-perpendicular profiles from each map.

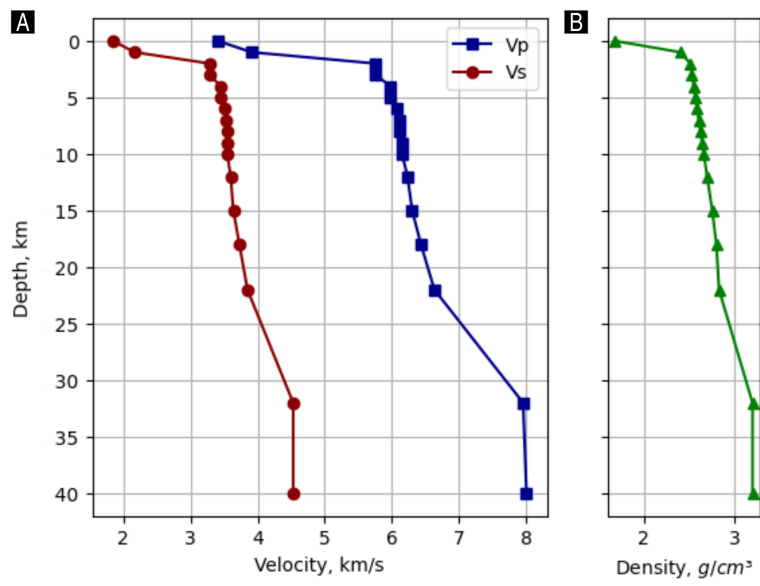


Figure S14: (A) P-wave velocity  $V_p$ , S-wave velocity  $V_s$  and (B) density  $\rho$  values used for the Green's functions computation for a stratified medium.  $V_p$  and  $V_s$  values from the surface down to 40 km-depth come from [Karabulut \(2024\)](#),  $\rho$  values from the surface down to 1.5 km-depth come from [Özalaybey et al. \(2011\)](#), and the other values of  $\rho$  are chosen according to Crust 1.0 ([Laske et al., 2013](#)).

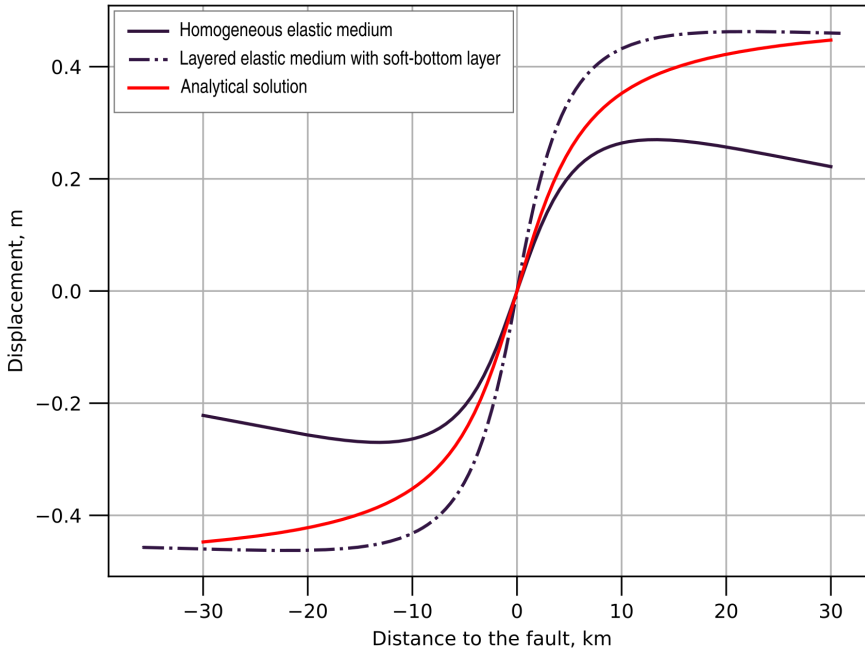


Figure S15: Perpendicular to the fault profiles of displacements based on different Green's functions, for homogeneous slip with amplitude of 1 cm starting from 5 km-depth. Displacements using the Okada (1985) solution are shown with a solid blue line computed using a 4060 km-length and 35 km-deep fault. The dash-dotted line is the result for the same fault geometry but using the velocity model shown figure Figure S14 and a soft medium below 35 km-depth. The red line corresponds to the analytical solution of a dislocation in an infinite half space following the equation  $d = \frac{s}{\pi} \cdot \text{atan}(\frac{x}{D})$  (Savage and Burford, 1970).

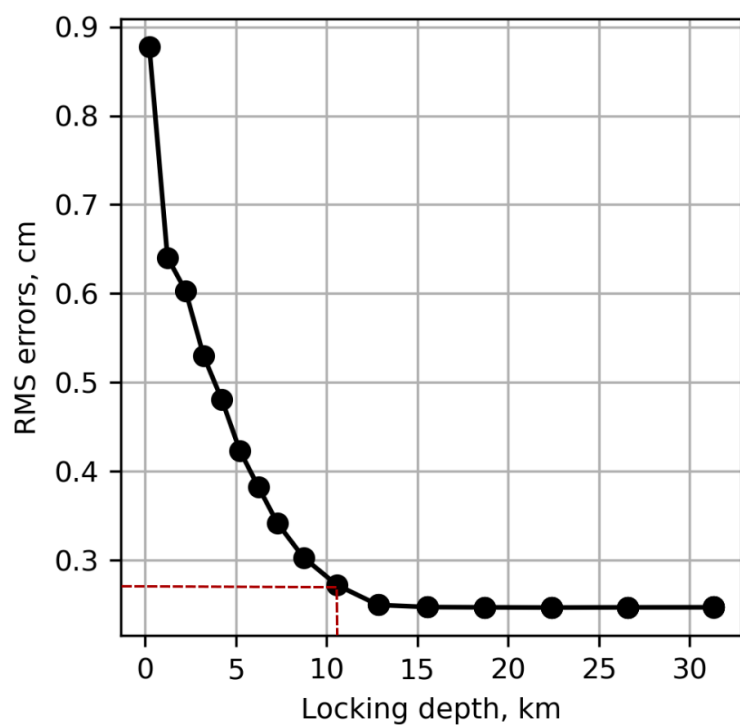


Figure S16: RMS errors as a function of the *a priori* locking depth. The *a priori* locking depth for the preferred model.

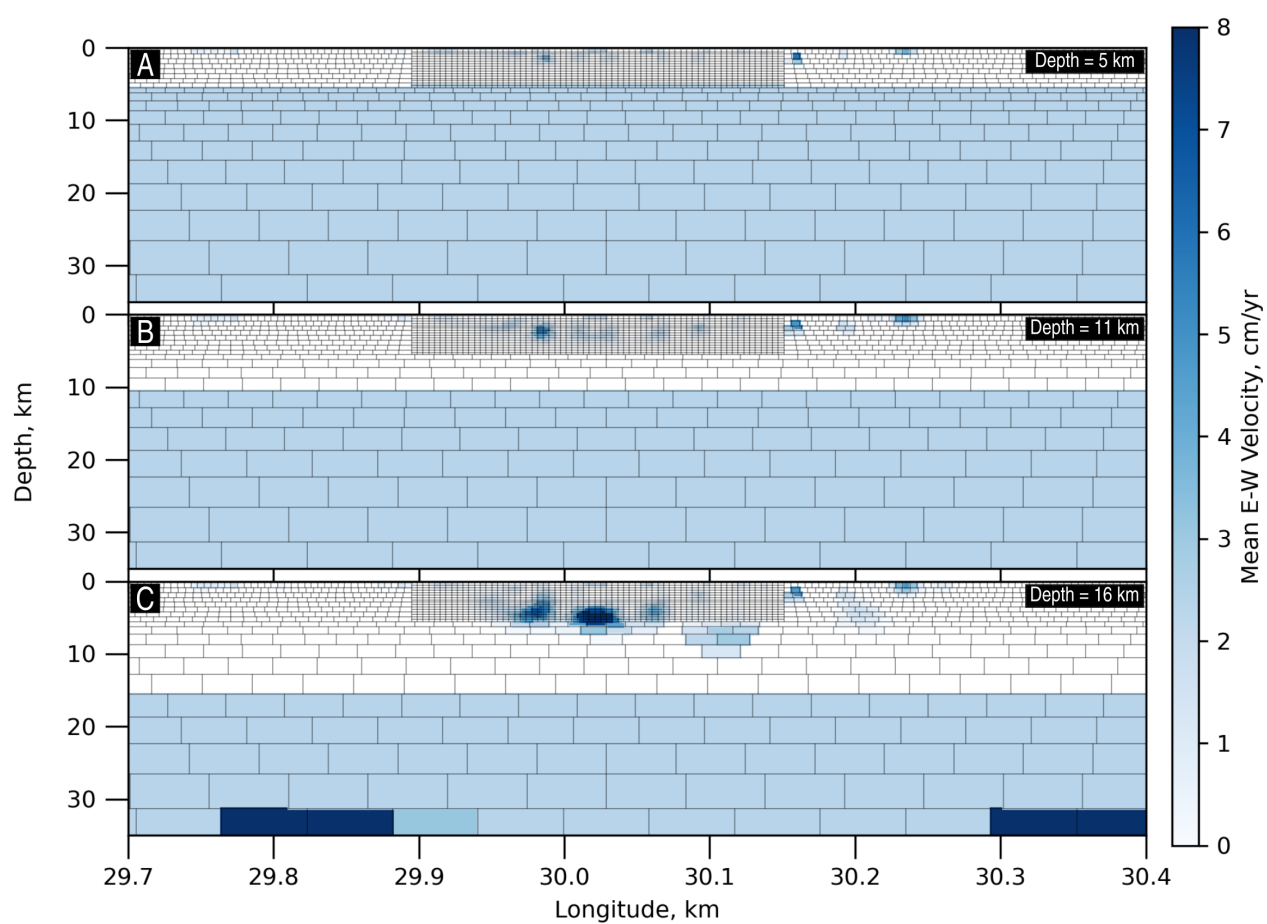


Figure S17: Slip distributions obtained using several *a priori* models with locking depths of (A) 5 km, (B) 11 km and (C) 16 km.

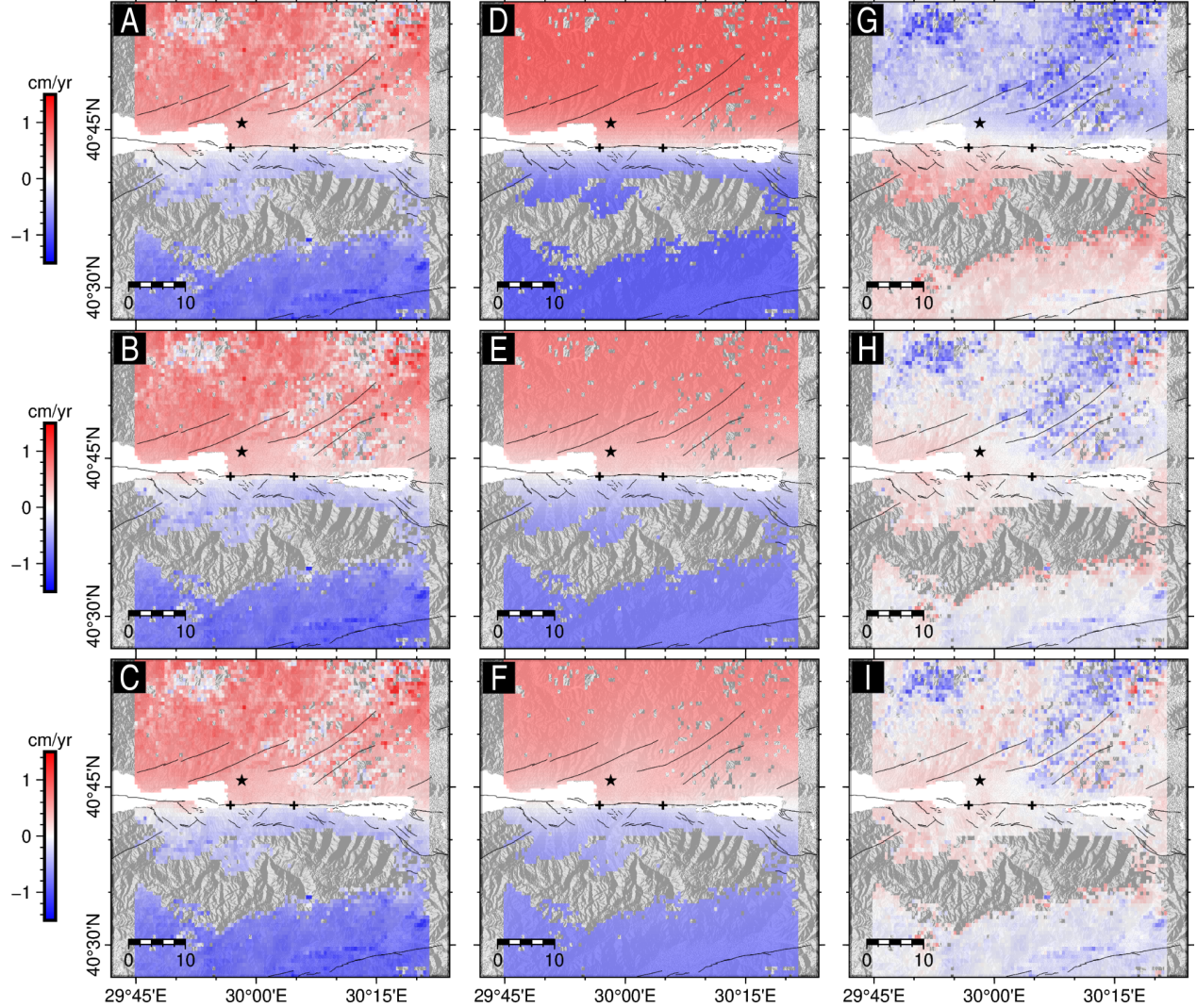


Figure S18: Comparison between the East-West steady creep velocity field (A-C) and three model predictions obtained from the inversions based on *a priori* models with the locking depths of (D) 5 km, (E) 11 km and (F) 16 km. The maps from G to I correspond to the difference between the data and the model predictions for each *a priori* model.

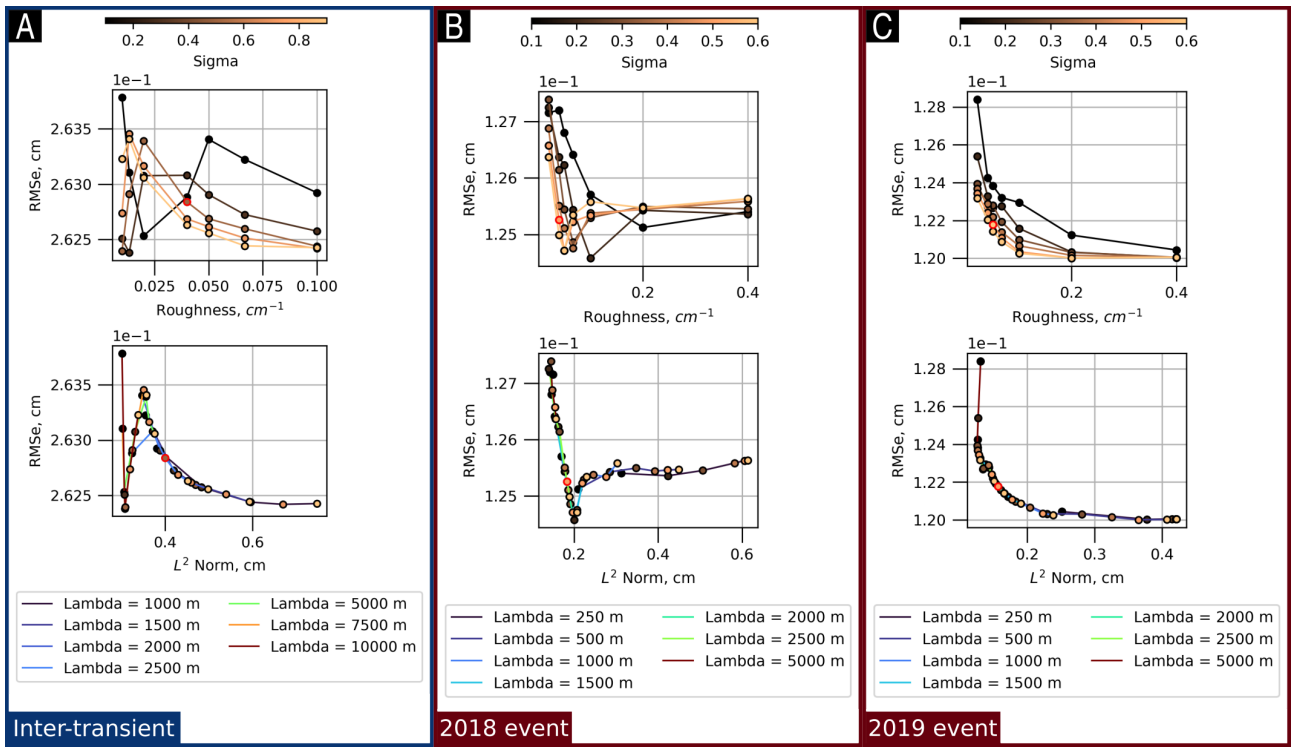


Figure S19: L-curves obtained for (A) the steady creep, (B,C) the 2018 and 2019 slow slip events, respectively. The top panels correspond to the RMS errors as a function of slip roughness, and the bottom panels correspond to the RMS errors as a function of the  $L^2$ -norm. The red dots indicate the inversion parameters chosen for each inversion.

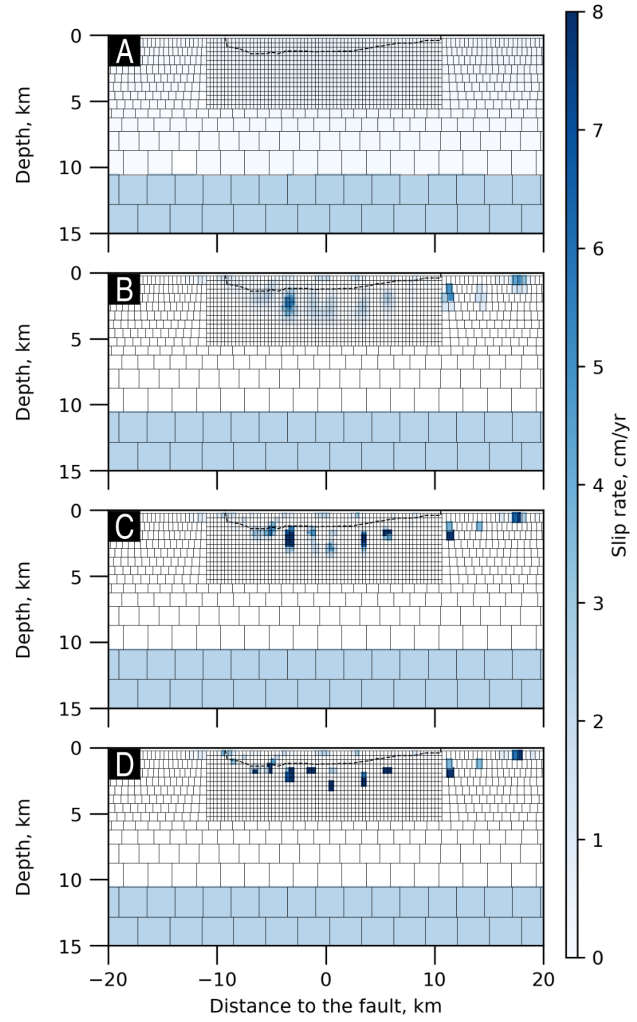


Figure S20: Slip distributions obtained from the inversions of the mean inter-transient velocity, for several parameters. Slip distributions obtained using the following couples  $(\lambda; \sigma_m)$ : (A) ( $\lambda = 10000$  m;  $\sigma_m = 0.1$ ), (B) ( $\lambda = 2000$  m;  $\sigma_m = 0.5$ ), (C) ( $\lambda = 1500$  m;  $\sigma_m = 0.7$ ) and (D) ( $\lambda = 1000$  m;  $\sigma_m = 0.9$ ).

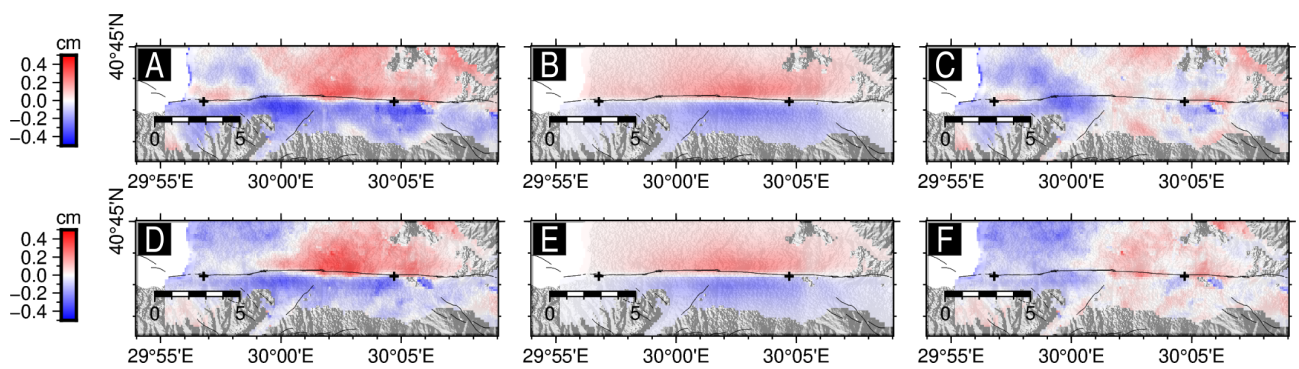


Figure S21: Comparison between the InSAR East-West displacements recorded during the 2018 (A) and 2019 (D) transient events with the model predictions (B,E respectively). The residual displacements are shown on maps C and F respectively.

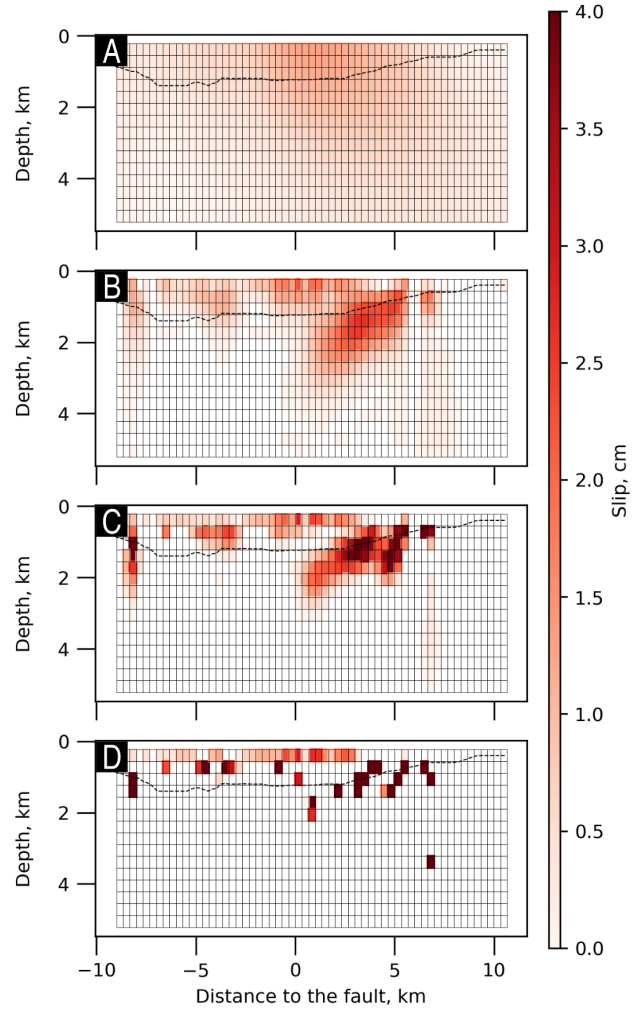


Figure S22: Slip distributions obtained from the inversions of the 2018 transient event displacements, for several parameters. Slip distributions obtained using the following couples  $(\lambda; \sigma_m)$ : (A)  $(\lambda = 5000 \text{ m}; \sigma_m = 0.1)$ , (B)  $(\lambda = 2000 \text{ m}; \sigma_m = 0.5)$ , (C)  $(\lambda = 1000 \text{ m}; \sigma_m = 0.4)$  and (D)  $(\lambda = 250 \text{ m}; \sigma_m = 0.6)$ .

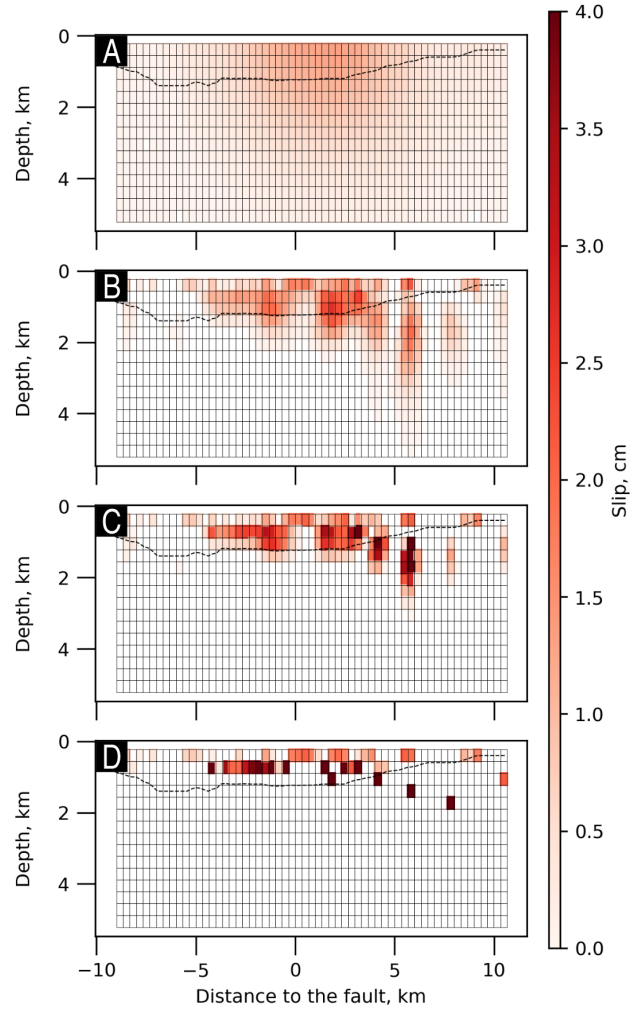


Figure S23: Slip distributions obtained from the inversions of the 2019 transient event displacements, for several parameters. Slip distributions obtained using the following couples  $(\lambda; \sigma_m)$ : (A)  $(\lambda = 5000 \text{ m}; \sigma_m = 0.1)$ , (B)  $(\lambda = 2000 \text{ m}; \sigma_m = 0.5)$ , (C)  $(\lambda = 1500 \text{ m}; \sigma_m = 0.7)$  and (D)  $(\lambda = 1000 \text{ m}; \sigma_m = 0.9)$ .

## 2 Discussion materials

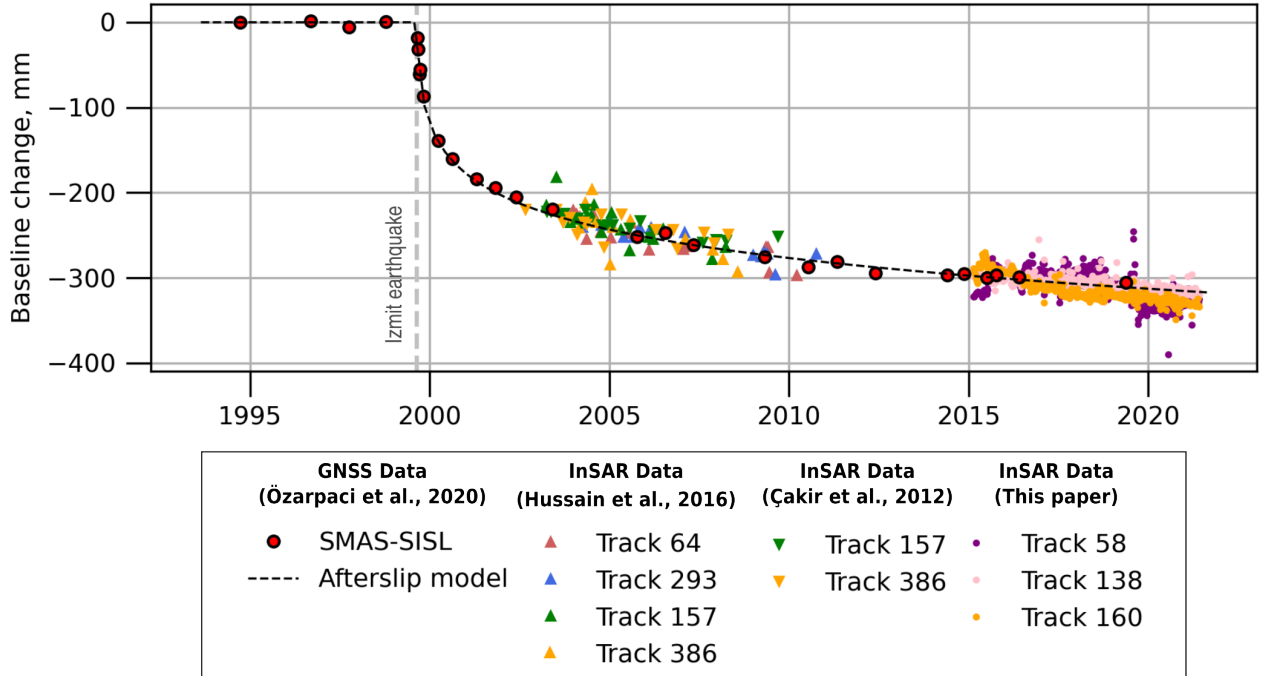


Figure S24: Comparison between the GNSS SMAS-SISL baseline and the InSAR results. The red dots correspond to the East-West component of the GNSS baseline, after the removal of the interseismic behavior with an overlaying afterslip model in black dotted line determined by [Özarpaci et al. \(2020\)](#). The InSAR data come from [Cakir et al. \(2012\)](#), [Hussain et al. \(2016\)](#) and our study.

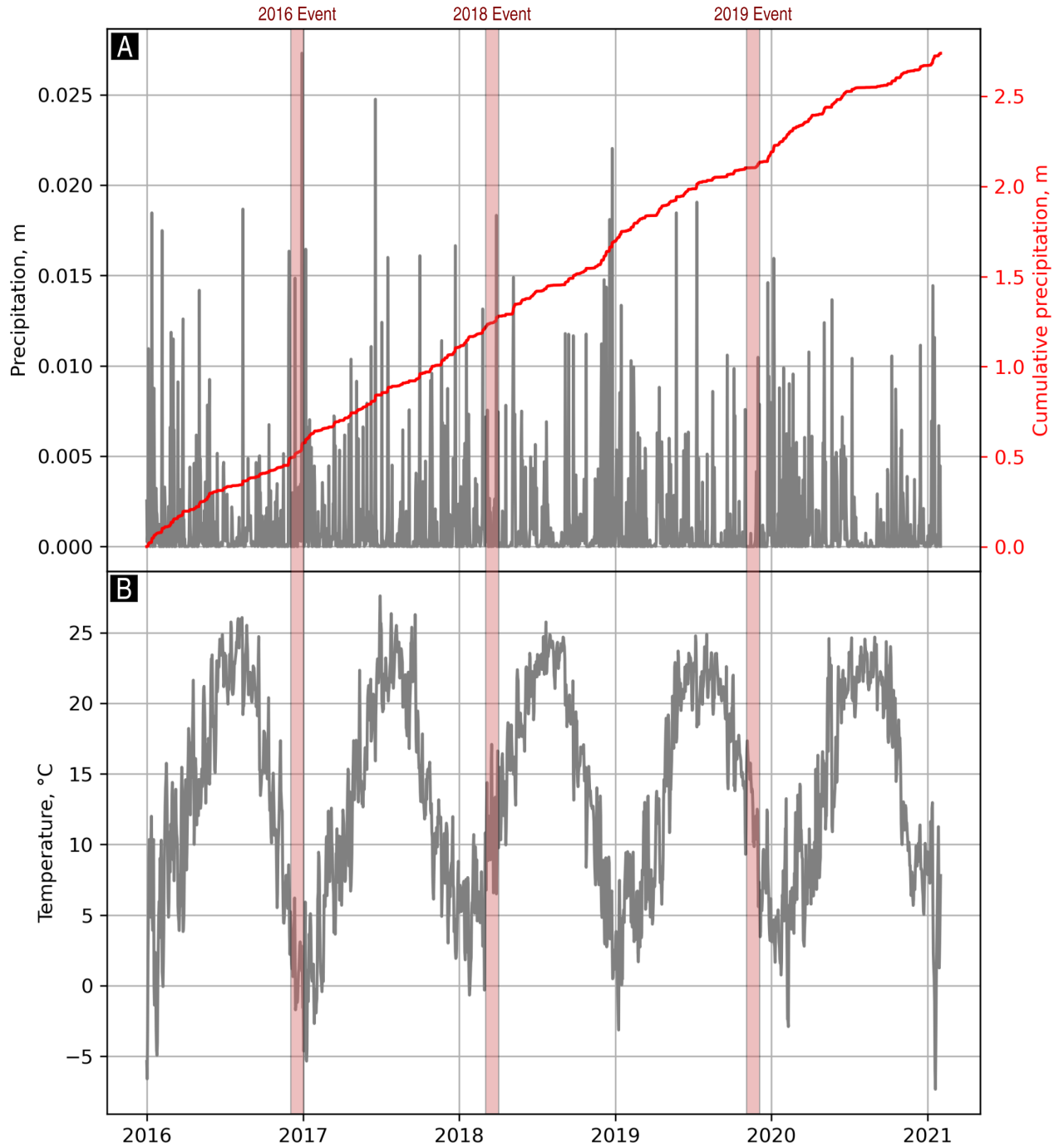


Figure S25: Meteorological data over the period 2016 – 2021 within the Izmit basin. These data come from the ERA-5 models, averaged on the region between the longitudes  $E029.8^{\circ}$  and  $E030.8^{\circ}$  and the latitudes  $N40.6^{\circ}$  and  $N40.9^{\circ}$ . (A) The daily precipitation is shown by the gray line, with the cumulative precipitation shown by the red line. (B) Time evolution of the daily temperature. The red periods correspond to the three slow slip events detected by InSAR.

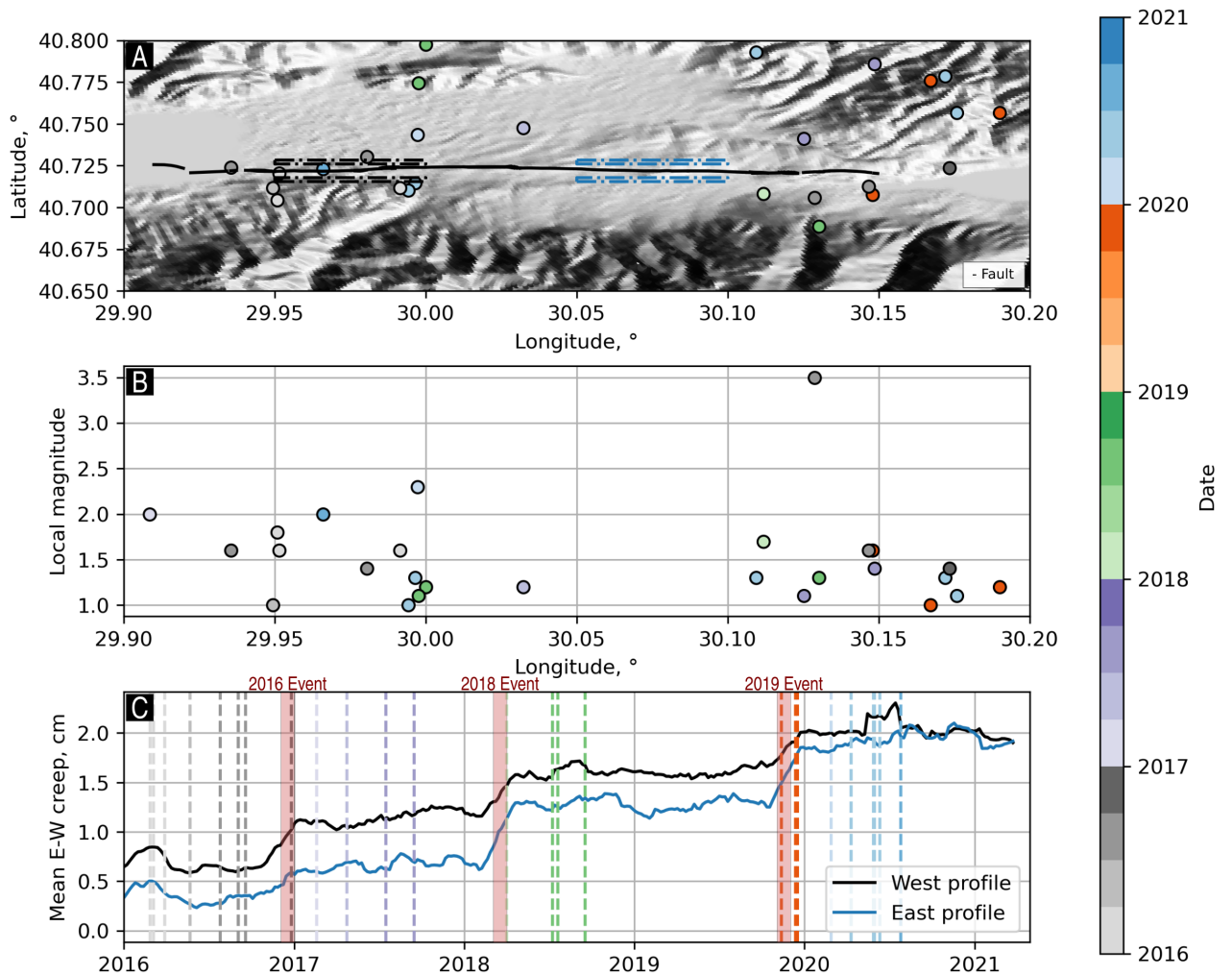


Figure S26: Seismic events from the AFAD catalog, from the January 1<sup>st</sup>, 2016 to the March 1<sup>st</sup>, 2021. (A) Location of the events within the Izmit basin. The dotted-dashed boxes correspond to the pixels used for the mean East-West creep profiles presented in the graph (C). (B) Local magnitude  $M_L$  as a function of longitude. (C) Time evolution of the mean East-West relative displacement located west (black line) and on the central part (blue line) of the Izmit segment. The dates of each event are represented by the coloured vertical dotted line. The red periods correspond to the three slow slip events detected by InSAR.

## References

- Barka, A., 2002. The Surface Rupture and Slip Distribution of the 17 August 1999 Izmit Earthquake (M 7.4), North Anatolian Fault. *Bulletin of the Seismological Society of America* 92, 43–60. URL: <https://pubs.geoscienceworld.org/bssa/article/92/1/43-60/102910>, doi:10.1785/0120000841.
- Cakir, Z., Ergintav, S., Ozener, H., Dogan, U., Akoglu, A.M., Meghraoui, M., Reilinger, R., 2012. Onset of aseismic creep on major strike-slip faults. *Geology* 40, 1115–1118. URL: <https://pubs.geoscienceworld.org/geology/article/40/12/1115-1118/130811>, doi:10.1130/G33522.1.
- Hussain, E., Wright, T.J., Walters, R.J., Bekaert, D., Hooper, A., Houseman, G.A., 2016. Geodetic observations of postseismic creep in the decade after the 1999 Izmit earthquake, Turkey: Implications for a shallow slip deficit: IZMIT CREEP. *Journal of Geophysical Research: Solid Earth* 121, 2980–3001. URL: <http://doi.wiley.com/10.1002/2015JB012737>, doi:10.1002/2015JB012737.
- Karabulut, H., 2024. High resolution p-wave tomography of the rupture zone of 1999 izmit and duzce earthquake. *Geophysical Journal International*, Submitted .
- Laske, G., Masters, G., Ma, Z., Pasyanos, M., 2013. Update on CRUST1.0 - A 1-degree Global Model of Earth's Crust .
- Okada, Y., 1985. Surface deformation due to shear and tensile faults in a half-space. *Bulletin of the Seismological Society of America* 75, 1135–1154. URL: <https://doi.org/10.1785/BSSA0750041135>, doi:10.1785/BSSA0750041135.
- Savage, J.C., Burford, R.O., 1970. Accumulation of tectonic strain in California. *Bulletin of the Seismological Society of America* 60, 1877–1896. URL: <https://pubs.geoscienceworld.org/bssa/article/60/6/1877/116823/Accumulation-of-tectonic-strain-in-California>, doi:10.1785/BSSA0600061877.
- Özalaybey, S., Zor, E., Ergintav, S., Tapirdamaz, M.C., 2011. Investigation of 3-D basin structures in the İzmit Bay area (Turkey) by single-station microtremor and gravimetric methods. *Geophysical Journal International* 186, 883–894. URL: <https://doi.org/10.1111/j.1365-246X.2011.05085.x>, doi:10.1111/j.1365-246X.2011.05085.x.

Özarpacı, S., Doğan, U., Ergintav, S., Çakır, Z., Özdemir, A., Floyd, M., Reilinger, R., 2020. Present GPS velocity field along 1999 Izmit rupture zone: evidence for continuing afterslip 20 yr after the earthquake. *Geophysical Journal International* 224, 2016–2027. URL: <https://academic.oup.com/gji/article/224/3/2016/5992340>, doi:10.1093/gji/ggaa560.